Laser ablation for structuring Li-ion electrodes for fast charging and its impact on material properties, rate capability, Li plating, and wetting

Nathan Dunlap [a], Dana B. Sulas-Kern [a], Peter J. Weddle [a], Francois Usseglio-Viretta [a], Patrick Walker [a], Paul Todd [a], David Boone [b], Andrew M. Colclasure [a], Kandler Smith [a], Bertrand J. Tremolet de Villers [a], Donal P. Finegan [a,*]

[a] National Renewable Energy Laboratory (NREL), 15013 Denver West Parkway, Golden, CO 80401, United States of America
[b] Clarios, 5757 North Green Bay Avenue, Florist Tower, Milwaukee, WI 53209, United States of America

HIGHLIGHTS

- Femtosecond pulsed laser ablation achieves high rate of material removal.
- Laser patterning process has minimal impact to remaining active materials.
- Laser patterning either electrode improves fast charge cycling performance.
- Laser patterns improve electrolyte wetting and reduce risk of Li-plating.

ARTICLE INFO

ABSTRACT

Laser ablation is a scalable technique for decreasing the effective tortuosity of electrodes by selectively removing material with high precision. Applied to ≈ 110 μm thick electrode coatings, this work focuses on understanding the impact of laser ablation on electrode material properties at the beginning of life and synergistic impacts of ablated channels on cell performance throughout their cycle life. Post laser ablation, local changes in chemistry, crystallography, and morphology of the laser-impacted electrode regions are investigated. It is shown that femtosecond pulsed laser ablation can achieve high-rate material removal with minor material damage locally at the interface of the impacted zones. The capacity achieved during a 6C (10 min) constant-current constant-voltage charge to 4.2 V improved from 1 mAh cm^{-2} for the non-ablated electrodes to almost 2 mAh cm^{-2} for the ablated electrodes. This benefit is attributed to a synergistic effect of enhanced wetting and decreased electrode tortuosity. The benefit was maintained for over 120 cycles, and upon disassembly decreased Li-plating on the graphite anode was observed. Finally, multi-physics modeling in conjunction with wetting analyses showed that laser ablating either one of the electrodes led to substantial improvements in wetting and rate capability, indicating that substantial performance benefits can be achieved by ablating only the graphite anode as apposed to both electrodes.

1. Introduction

For widespread adoption of electric vehicles, Li-ion batteries need to achieve energy densities of 275 Wh/kg, cost less than $100/kWh and charge quickly (80% within 15 min) [1]. By increasing electrode thicknesses, clear opportunities exist for enhancing cell energy densities while reducing costs. Doubling the thickness of a cell's electrodes from 50 μm to 100 μm can increase its energy density 16%, while reducing costs by 30% [2]. These benefits arise from increasing the ratio of active to inactive material within the cell. However, increased loading is often accompanied by decreased Li-ion transport across the thick electrodes.

This leads to significant lithium concentration gradients from separator to current collector that can reduce the electrodes' accessible capacities and promote irreversible lithium plating [3,4].

Modeling conducted at the National Renewable Energy Laboratory (NREL) has explored the fast-charge limitations of planar electrodes and the impact of micro-features on ion-transport [5–9]. Secondary-pore networks (SPN), also called dual-pore network, were found to significantly reduce electrode tortuosity, improving their energy density and rate performance [8,9]. To date, researchers have utilized various techniques to engineer electrode architectures with voids or

---

macro-pores tailored to promote electrolyte wetting and improve Li-ion transport. These methods include co-extrusion [10,11], magnetic alignment of particles [12–14], controlled mud-cracking [15], freeze casting [16–19] and pore former inclusion [20]. A review of these various processes is available in [8].

Recently, short-pulsed lasers have been used to ablate micro-pores or channels into various Li-ion battery electrodes [21–23]. These laser patterned microstructures provide low tortuosity pathways for facile Li-ion transport deep into the electrode, limiting electrolyte concentration gradients and reducing the electrochemical overpotentials that lead to lithium plating. Research has shown that laser patterning a full cell's graphite anode can significantly improve its fast-charge performance [24–26]. Additionally, laser patterning both anode [27] and cathode [21] sheets has been linked to improved electrolyte wetting. To date, laser patterning has been shown to be compatible with LiFePO$_4$ (LFP) [22,28,29], LiMn$_2$O$_4$ (LMO) [23] and LiNi$_x$Mn$_y$Co$_z$O$_2$ (NMC) [30,31] cathode chemistries as well as extremely thick (>650 μm) electrode coatings [32]. In this work, simulation models and experimental techniques are combined to characterize thick (>100 μm), commercially relevant, laser patterned graphite anodes and NMC622 cathodes.

2. Experimental

2.1. Electrode materials

The electrodes used in this study were prepared by the Cell Analysis, Modeling, and Prototyping (CAMP) Facility at Argonne National Laboratory (Figure S1). Anodes were composed of 91.83 wt% graphite (Superior SLC1520P), 2 wt% C45 carbon (Timcal), 6 wt% polyvinylidene fluoride (PVDF) binder (Kureha 9300) and 0.17 wt% oxalic acid with a 15-μm-thick copper foil. Cathodes were prepared with 90 wt% NMC622 (ECOPRO), 5 wt% C45 carbon (Timcal) and 5 wt% PVDF binder (Solvay 5130) with a 20-μm-thick aluminum foil. After casting, the anode and cathode sheets were calendared to target porosities of 36.2% and 34.0%, respectively. This corresponds to coating thicknesses and mass loadings of 101 μm, 13.97 mg/cm^2 (anode) and 112 μm, 30.24 mg/cm^2 (cathode). Assuming active material specific capacities of 340 mAh/g (graphite) and 169 mAh/g (NMC622, 4.2 V vs. Li), the pristine anode and cathodes show large theoretical areal capacities of 4.35 mAh/cm^2 and 4.28 mAh/cm^2, respectively (Table S1).

2.2. Laser patterning

The pre-calendared electrodes were patterned with a bench-top laser system (Figure S2). A diode-pumped solid-state femtosecond laser (Advanced Optowave FEMTO-IR-1030) with a 1030 nm emission wavelength (λ) provided $\approx$ 600 fs laser pulses with tunable repetition rates between 100 kHz–1 MHz and average power of $\leq$11 W at 100 kHz (Table S2). A high-speed scanning system with galvanometer-controlled mirrors (Aerotech, Inc.) and an f-theta lens was used to direct and focus the laser beam to a $\approx$25 μm spot size [33]. Electrode ablation was carried out in ambient air under a directed flow of nitrogen gas. A vacuum exhaust tube was positioned close to the electrode surface to remove ablated materials, preventing their re-deposition.

Continuous linear channels (i.e., grooves) were ablated into both anode and cathode sheets. Continuous channels were chosen over more complex patterns because they could be easily produced with conventional roll-to-roll electrode manufacturing processes, for example, with the use of diffractive optical element beam splitters. To ablate the channels, a laser power of 0.6 W and a pulse repetition rate of 100 kHz were used for both anodes and cathodes. Translating these parameters to a modern roll-to-roll manufacturing process, we predict that a high-power 300 W laser could simultaneously cut $\approx$600 trenches into a 118 mm wide electrode at a rate of up to 10 m/min.

After patterning, the bench-top laser system was used to cut 14 mm diameter anode and cathode disks from their respective electrode sheets. Two 1 mm diameter circular areas were ablated along the electrodes' edges (Figure S3), exposing the current collector and allowing the electrodes to be spot welded (Sunstone CD160 DPM2) to 0.5 mm thick (15.4 mm diameter) stainless steel coin-cell spacers to reduce their contact resistances. Considering these spot welding points, each electrode disk had a total coated surface area of $\approx$1.52 cm^2.

2.3. Scanning Electron Microscopy (SEM) and Energy Dispersive X-ray Spectroscopy (EDS)

The laser patterned electrodes were imaged with a scanning electron microscope (SEM, Hitachi S-4800, Nova NanoSEM 630). A Joel IB-09010CP cross section polisher was used to gain an unobstructed view of the ablated channel geometry. Energy dispersive X-ray spectroscopy (EDS) (Oxford Ultima Max) was used to measure the chemical composition of the patterned electrodes' cross sectioned surfaces.

2.4. Powder X-ray diffraction (PXRD)

Powder X-ray diffraction (PXRD) scans were made with a Rigaku Ultima IV diffractometer using Cu Kα radiation. Full electrode disks were mounted on amorphous silicon wafers to reduce background interference. The lattice parameters and peak shapes of the electrodes' active materials and current collectors were refined using the Rietveld method.

2.5. Cell preparation

Coin-cells were assembled in the dry atmosphere of an argon filled glove box (MBRAUN LABmaster 130) with oxygen and moisture content controlled below 1 ppm. Single 3/4" diameter punches of Celgard 2500 (25 μm, 55% porosity) were used to mechanically and electrically separate the electrodes. Each coin-cell was flooded with 1.2 M LiPF6 in ethyl carbonate/ethyl methyl carbonate (EC:EMC, 3:7 w/w, Tomiyama, Japan), referred to as "Gen2" electrolyte, before being crimped closed. Full-cells comprising all four combinations of laser patterned (L) and pristine (P) anodes and cathodes were constructed. These combinations will be referred to as CPAP, CLAP, CPAL and CLAL, with "C" referring to cathode and "A" referring to anode. For example, CPAL refers to a coin cell made with a pristine cathode and a laser patterned anode. In the case of the CLAL cell, care was taken to align the laser patterned channels on the anode and cathode during assembly. This was done by aligning the weld points which were positioned in line with the laser patterned channels. Ideally, the anode channels would be positioned directly atop the cathode channels. However, this is impossible to achieve by hand during coin cell assembly. In reality, the anode and cathodes are positioned such that their respective channels are close to parallel to each other without the expectation of true overlapping alignment.

2.6. Electrochemical testing

To evaluate the thick electrodes' fast charge (6C) capabilities, a series of full-cells were cycled per United States Department of Energy (USDOE) battery-testing guidelines [34]. All cells were cycled at room temperature (24 °C) using a MACCOR Series 4000 (Maccor Inc.) battery cycler. Cycling current densities were calculated from the theoretical capacity of a pristine (CP) cathode disk (Table S1). The same current densities were used for each coin-cell configuration, even those containing laser patterned cathodes (CLAP & CLAL). After assembly, each coin-cell underwent the following formation process:

  (i) Tap charge to 1.5 V and hold for 15 min,
 (ii) Rest at open-circuit voltage (OCV) for 12 h

(iii) 3 cycles at C/10 with constant-voltage (CV) hold at 4.2 V until current falls below C/20

(iv) 3 cycles at C/2 with constant-voltage (CV) hold at 4.2 V until current falls below C/20

Next, the cells were subjected to one hundred 6C CC–CV fast-charge cycles. The details of the fast-test are outlined in Table S3 and explained below. Each fast-charge cycle begins with a 6C (25.84 mA/cm^2) constant-current (CC) charge until the upper voltage limit (4.2 V) is reached. Next, the cell is held at 4.2 V (CV) until that cycle's total charge time (CC + CV) reaches 10 min. Following charging, the cell is allowed to rest for 15 min while its open-circuit-potential (OCP) is recorded. The cells are then fully discharged at a CC C/2 rate followed by a CV hold at 3.0 V (I < C/10). Following discharging, the cell was again allowed to rest for 15 min before proceeding on to the next 6C fast charge step. After 25 consecutive fast-charge cycles, the cells were subjected to 3 C/2 CC–CV (<C/10 current limit) cycles to quantify their capacity loss. After completing one hundred 6C fast charge cycles, the cells were transferred into a glovebox for disassembly and postmortem analysis.

To enable the fitting and validation of a COMSOL Multiphysics electrochemical model (Section S2), CPAP coin cells were subjected to the asymmetric step-charge rate-test outlined in Table S4. The cells were cycled at room temperature (24 °C) using a MACCOR Series 4000 (Maccor Inc.) battery cycler. Cycling current densities were calculated from the theoretical capacity of a pristine (CP) cathode disk (Table S1).

2.7. Electrochemical impedance spectroscopy

Following one hundred 6C CC–CV fast charge cycles, the fully discharged full-cell coin-cells were subjected to electrochemical impedance spectroscopy (EIS) sweeps (1 MHz–10 mHz, 10 mV vs OCV) using a Metrohm Multi Autolab M204.

To quantify the rate and degree of electrode wetting [35], EIS scans (1 MHz–10 mHz, 10 mV vs OCV, Metrohm Multi Autolab M204) were made on CPAP, CPAL and CLAL coin cells immediately following their assembly. Additional EIS scans were then taken periodically over the following 48, while the cells rested at 25 °C. Each cell's total wetted/electrochemically active surface area was calculated using their double layer capacitance, which was determined by fitting their Nyquist plots with a modified Randles circuit.

3. Results and discussion

3.1. Laser patterning

Preliminary testing showed that channel depth and width at the electrode surface scaled with the incident beam power, with higher beam powers producing deeper, wider channels. However, the channel angle is caused by the incident beam shape and was expected to remain relatively constant around 75° regardless of the beam power (Figure S4).

To limit capacity loss, the total cathode mass loss was constrained to ≈10 wt% during patterning. While removing more material would result in further improved Li-ion transport in the electrode, it comes at the price of reduced volumetric energy density and loss of costly active materials. Therefore, a mass loss limit of 10 wt% was arbitrarily selected as plausibly realistic constraint for industrial viability. With this mass loss constraint considered, electrochemical modeling predicted optimal fast-charge performance from parallel channel patterns with relative depths ≈50% of the electrode coating thickness, spaced ≈100 μm apart. After patterning, actual mass losses were found to be ≈11.6% and ≈16.1% for the cathode and anode disks, respectively (Table S1). This corresponds to ≈10.9% (cathode) and ≈16.9% (anode) losses in the electrodes' theoretical capacities due to channel ablation.

This discrepancy between expected and observed mass losses will be discussed in detail below.

Figs. 1(a,b) and (g, h) show top-down SEM images of the laser patterned cathode and anode surfaces, respectively. There are no signs of residual debris on either electrode after patterning. FIB-SEM cross sectional images of the laser patterned cathode and anode are shown in Figs. 1(c–f) and (i–l), respectively. From these images, cathode channel dimensions were measured to be ≈36 μm wide and ≈62 μm deep (55% total thickness), while the anode channels were found to be ≈45 μm wide and ≈49 μm deep (49% total thickness). From the top-down view, the edges of the cathode channels appear relatively smooth and uniform while the anode channel walls are more unevenly textured. The FIB-SEM cross sections show that the fast pulsed laser cracks and cleaves the polycrystalline NMC622 particles along their many grain boundaries (Fig. 1e, f) producing uniform channels with ≈75° symmetric walls. Conversely, entire graphite particles can be seen protruding far out from the edges of the anode channels, seemingly untouched by the laser (Fig. 1i). This observation agrees with previous reports on laser patterned NMC cathodes and graphite anodes [25,36,37]. The non-uniform ablation of the anode's graphite particles will be discussed in detail later, but the resulting irregularity in the ablated trench geometry could help account for the larger than expected mass losses in the laser patterned anodes. Additional mass losses could be attributed to unintended ablation of current collector foil during the preparation of the electrodes' spot welding points. Because the density of the anode's copper current collector is much larger (≈6.5X) than the electrode coating (1.38 g/cm^3), any material removed from the copper foil would lead to a disproportionate overestimation of graphite mass loss with patterning. This hypothetical overestimation would not be as significant for the cathode, as the density of the aluminum current collector foil and cathode coating are both ≈2.70 g/cm^3.

3.2. Laser induced electrode damage

Beyond the general geometry of the patterned channels, it is important to understand the residual impact laser ablation has on the electrode materials. Femtosecond pulsed lasers are specifically used in electrode patterning because the extremely short duration of their pulses produces ablation with minimal heat input to the surrounding material. However, both graphite and metal oxide active materials are known to temporarily melt under fast pulsed laser exposure at ambient pressures suggesting residual damage, disorder and inhomogeneities could persist near the ablated channels [30,38–43]. Therefore, both electrodes should be probed for chemical and structural changes following laser patterning.

Fig. 2a illustrates a multi-elemental EDS map of a cross sectioned, laser patterned NMC622 cathode. Light-green NMC particles are clearly highlighted, surrounded by a dark matrix of carbon-based conductive additives and binder. Single-element EDS maps (Figs. 2b–g) further accentuate the metal-oxide particles and carbon matrix. However, there are no clear signs of any compositional or structural irregularities along the laser ablated channels of the cathode. To further quantify the chemical composition of the patterned cathode, six EDS point scans were made both near to and away from the laser ablated channels. The full result of each point scan is included in the supplementary section (Table S5). The relative atomic percentage of each element, normalized to the measured nickel content, are grouped according to their corresponding component within the cathode in Figure S6. This data shows that the relative atomic ratio of Ni, Mn and Co remains around 6:2:2 regardless of the proximity to the laser ablated channel, suggesting that the laser ablation process has little impact on the stoichiometry of the cathode's remaining NMC622 particles.

EDS maps (Figure S5) and point scans (Table S6) of a patterned anode are included in the supplementary information section. There are no signs of compositional or structural variations in the anode due to the laser ablation process.
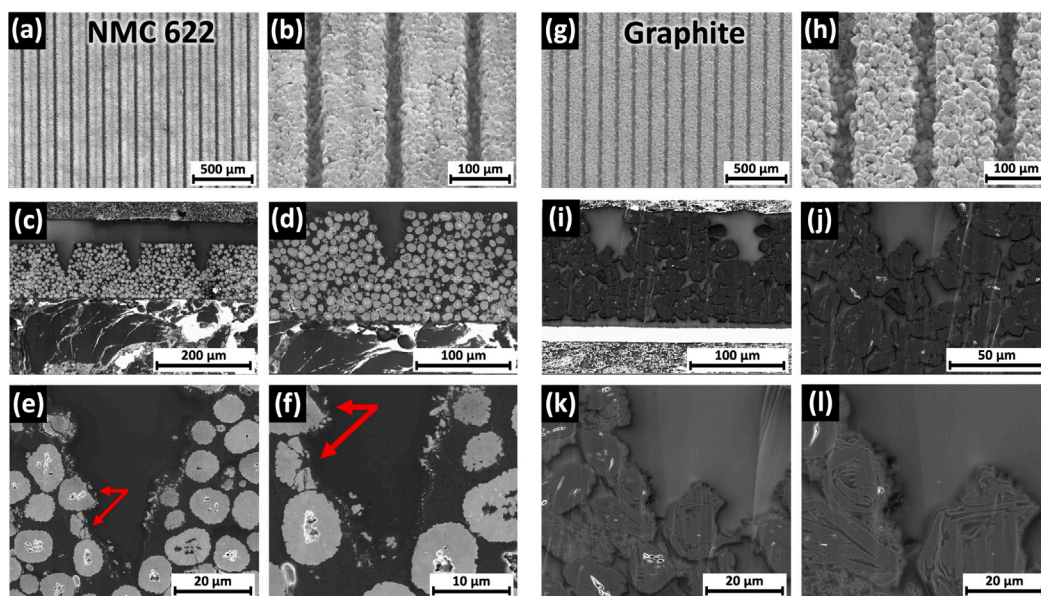
Fig. 1. Top-down SEM images of laser patterned (a, b) NMC622 cathode and (g, h) graphite anode sheets. FIB-SEM cross sectional images of laser patterned (c–f) NMC622 cathode and (i–l) graphite anode. Note, the fibrous material above and below the cross sectioned electrodes (c–d, i–j) is an artifact of sample preparation and not a part of the electrodes.
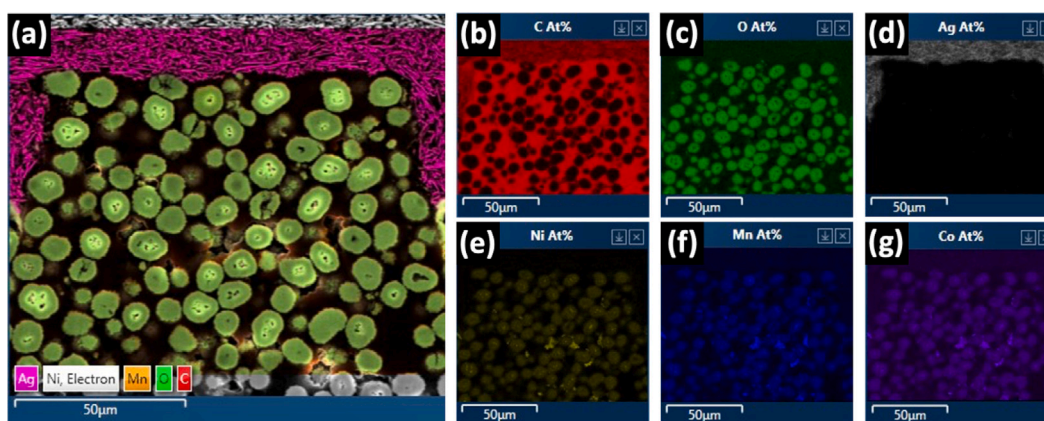

Fig. 2. (a) FIB-SEM cross sectional image of a laser ablated NMC622 cathode. (b–g) EDS maps of the cross sectioned cathode. The purple Ag layer along the upper edge of the cathode is an artifact of sample preparation and not apart of the electrode. (For interpretation of the references to color in this figure legend, the reader is referred to the web version of this article.)

Next, the crystalline structure of the anode and cathode active materials were probed with powder X-ray diffraction (PXRD). The diffraction spectra of full cathode and anode disks before and after laser patterning along with the spectra of their corresponding current collector foils are plotted in Fig. 3.

The pristine cathode's spectra (Fig. 3a) shows clearly split (006) /(102) and (108)/(110) peaks. This is a sign that the NMC622 active material is of good quality with a highly crystallized layered structure [44]. No new peaks developed in the cathode's spectra after patterning, indicating that no new crystalline phases formed during the ablation process. Figs. 3b–d highlight the NMC622 crystal's three largest peaks. The patterned electrode's peaks match the unpatterned electrode's, with no significant shifting or broadening. A small degree of $K_{\alpha 1}$–$K_{\alpha 2}$ splitting was observed in the (101) and (104) Bragg peaks. This alludes to an increased degree of crystallinity and grain size in the NMC near the cathode's channels after patterning [45].

Rietveld refinements were performed on the full XRD spectra (10–80 deg.) of the patterned and pristine cathode disks assuming a hexagonal layered phase in the R-3 m space group (α-NaFeO$_2$ structure). The fits, plotted atop the experimentally collected spectra, are displayed

Table 1
Crystallographic data for pristine and patterned NMC622.

Cathode	a (Å)	c (Å)	$c/(3a)$	Avg. Xtal size FWHM (nm)	Avg. Xtal size IB (nm)
Pristine	2.86965	14.2193	1.6517	122	132
Patterned	2.86971	14.2184	1.6515	163	228

Table 2
Crystallographic data for graphite.

Anode	a (Å)	c (Å)	Avg. Xtal size FWHM (nm)	Avg. Xtal size IB (nm)	Preferred orientation
Pristine	2.462	6.712	48	68	(0 0 1)
Patterned	2.462	6.710	204	285	(0 0 1)

in Figure S7. The structural information obtained from the refinement results are summarized in Table 1.

The measured NMC622 lattice constants agree well with the literature and vary insignificantly after laser patterning [46,47]. This suggests that the laser patterning had no detrimental impact on the structure of the residual NMC particles. High temperature exposure can
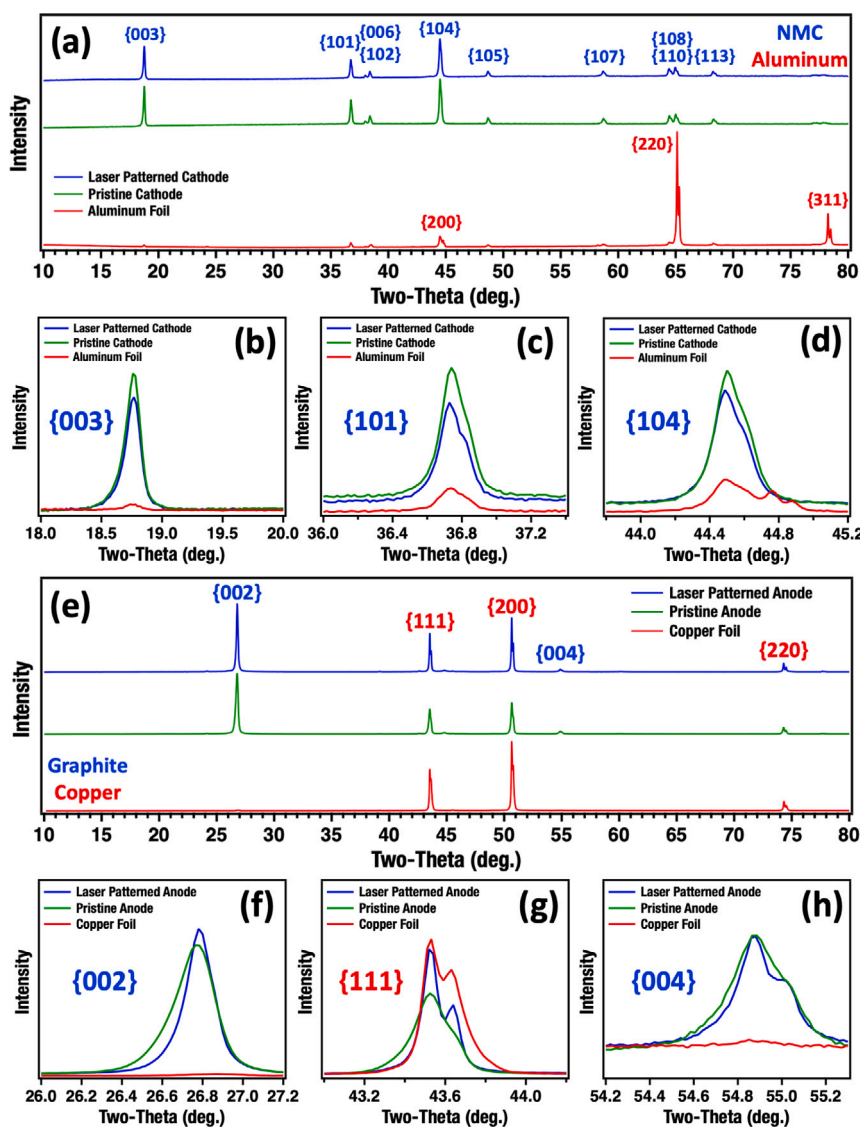
Fig. 3. PXRD spectra of pristine and laser patterned (a–d) cathode and (e–h) anode disks. Spectra of each electrode's respective current collector foil are included for reference.

result in cation (e.g. Li/Ni) disordering in NMC cathode materials [48]. This disordering can accelerate undesirable transition metal dissolution into the electrolyte, which can be exacerbated during high temperature or high voltage cycling [49]. This should be a significant point of focus for laser patterned NMC based cathodes, as the exposed surfaces of the ablated architectures present large areas of possibly heat-affected material for reaction with electrolyte. Previous reports have used the c/3a ratio as an indication of cation ordering in NMC [45,47]. A c/3a value of 1.633 is associated with a pure cubic close packed rock salt structure in which Ni and Li atoms are fully disordered between the 3a (lithium layer) and 3b (transition metal layer) sites. The large c/3a values (>1.65) calculated from the Rietveld fits indicate a highly ordered structure both before and after patterning with negligible lithium loss and cation disordering due to high temperature exposure during the laser patterning process. This supports the claim that the use of femtosecond pulsed lasers for patterning results in minimal damage to residual materials due to rapid heat dissipation during ablation. Interestingly, the size of coherently scattering crystalline domains calculated with either the Scherrer or Stokes & Wilson methods show an increase in average NMC crystallite size after laser patterning. This indicates that the regions surrounding the laser ablated channels experienced a measurable degree of laser-induced annealing during patterning.

The pristine and patterned anodes' XRD spectra also overlap closely (Fig. 3e). Large peaks associated with the electrodes' copper current collectors are present in the spectra of both the patterned and pristine disks (Fig. 3g). This is because both electrodes were prepared with spot weld points exposing sections of their current collector. After patterning, the major graphite peaks sharpen (Fig. 3f, h), marking an increase in crystal domain size.

The anode's full XRD spectra were also fit with the Rietveld method (Figure S7). The structural information calculated from the refinements are listed in Table 2. The graphite lattice constants are consistent with the literature [50] and do not change with patterning. This suggests that the laser ablation process did not produce significant defects in the remaining graphite particles, although other methods (e.g., Raman spectroscopy) would be more effective at quantifying defects in the graphite's layered structure. After patterning, the anode's average graphite crystal domain grew significantly, while maintaining a (001) preferred orientation. This indicates that the ultra-fast laser pulses had an annealing/aggregating like effect on the remaining graphite particles [51–53].

The irregularity of the anode channels could be explained by the orientation and size of their oblong graphite particles. Graphite displays significant anisotropy in its mechanical and thermal properties due to its layered, planar structure. Because of very weak bonding between
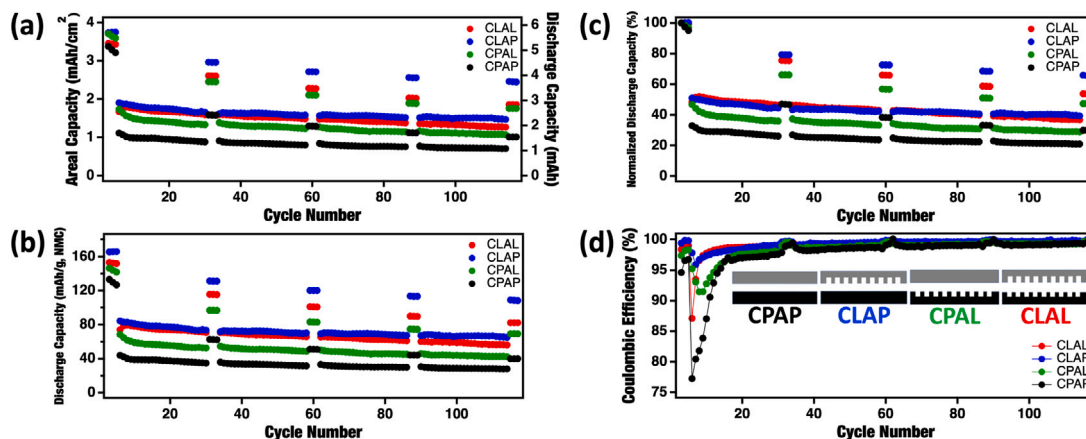
Fig. 4. Coin cell discharge capacity normalized to (a) electrode area, (b) cathode active material loading and (c) first cycle discharge capacity. (d) Coin cell coulombic efficiency and visualization of the coin cell naming scheme. CPAP refers to a full cell constructed with both a pristine anode and cathode. CLAP refers to a cell where a laser patterned cathode is paired with a pristine anode. CPAL refers to a full cell constructed with a pristine cathode and a laser patterned anode, while CLAL represents a cell containing both a laser patterned cathode and a laser patterned anode. All plots begin on the cell's 1st C/2 cycle, which is their 4th total cycle after formation.

neighboring planes, the c-axis {001} thermal conductivity is very small compared to the in-plane {100} value [39]. As the incident beam impacts the (001) oriented surface of the onion-like graphite, the laser's energy would largely travel transversely along the direction of the particles outermost layers (Figure S4b), rather than down and through the particle. This would result in the sequential ablation of the particles' outermost graphite layers culminating in total particle removal. The rough texturing of the anode channels could then be explained by this total graphite particle removal rather than the particle cleaving observed in the NMC622 active materials. Furthermore, the variability of the anode channel cross-sectional geometries could be accounted for by the variability in the size and orientation of the oblong graphite particles directly in the path of the incident beam during patterning.

3.3. Electrochemical performance

3.3.1. Fast-charge capacity

The fast charging capability of each electrode pairing was evaluated with the CC–CV charge protocol outlined in Table S3. Fig. 4 plots each cell's discharge capacity normalized to its cathode area (Fig. 4a), its cathode active material loading (Fig. 4b) and its first C/2 cycle discharge capacity. Each cell's first formation cycle (C/10) charge capacity, final 6C capacity and end-of-test (C/2) capacity retention are listed in Table 3.

The cells containing patterned electrodes showed significant utilization of their NMC622 cathode materials. The CLAP cell achieved the largest first cycle specific charge capacity (187.4 mAh/g, NMC) during formation (C/10), while the CLAL and CPAL cells achieved slightly smaller capacities of 181.7 mAh/g (NMC) and 180.8 mAh/g (NMC), respectively (Table 3). The fully pristine CPAP baseline cell achieved a notably smaller specific charge capacity (166.8 mAh/g, NMC) despite the C/10 CC–CV (I < C/20 cutoff) cycling conditions.

The cells' first CC charge and discharge voltage profiles are plotted in Fig. 5a. Even at the slow rate of C/10, the CPAP cell shows a significant overpotential on both charge and discharge in comparison to the cells containing laser patterned anodes and cathodes. This overpotential is represented by a peak shift in the cell's incremental capacity (dQ/dV) plot (Figure S9). It is also manifested by a large rest-step voltage-relaxation (35 mV) following the initial charge (Figure S10a). In fact, each cell's initial rest-step voltage-relaxation trends with the shifting of their first incremental capacity peak (≈3.55 V). The cells with the smallest first-charge overpotentials were those with laser patterned anodes, pointing towards improved ion-transport into the anode resulting in more uniform lithiation. The large overpotential and low capacity achieved by the CPAP cell during C/10 CC–CV cycling

Table 3

Coin cell cycling capacities and capacity retentions.

Cell	1st Charge capacity (C/10)	100th Charge capacity (6C)	Capacity retention (C/2)
CPAP	6.44 mAh 4.22 mAh/cm^2 166.8 mAh/g, NMC 74.5% C.E.	1.09 mAh 0.71 mAh/cm^2 28.2 mAh/g, NMC	30.0%
CLAP	6.45 mAh 4.23 mAh/cm^2 187.4 mAh/g, NMC 86.0% C.E.	2.24 mAh 1.47 mAh/cm^2 65.2 mAh/g, NMC	65.5%
CPAL	6.98 mAh 4.58 mAh/cm^2 180.8 mAh/g, NMC 85.2% C.E.	1.64 mAh 1.08 mAh/cm^2 42.5 mAh/g, NMC	46.2%
CLAL	6.25 mAh 4.10 mAh/cm^2 181.7 mAh/g, NMC 85.5% C.E.	1.94 mAh 1.28 mAh/cm^2 56.5 mAh/g, NMC	52.9%

cannot be attributed to sluggish ion-transport alone and suggests that its thick (>100 μm), unpatterned electrodes were unable to be fully wetted by electrolyte within the coin cell. This hypothesis will be tested in a following section.

It is interesting that while the fully pristine CPAP cell seems to suffer from critical wetting issues, both the CPAL and CLAP cells, which also contain unpatterned electrodes, show virtually no negative effects. Intuitively, one would expect the pristine electrodes in the CPAL and CLAP cells to achieve a lesser degree of wetting than their laser patterned counterparts, limiting the coin-cell's cycling performance. However, the cycling data shows that this is not the case, as the CPAL and CLAP cells achieve initial NMC-specific charge capacities as large as, if not larger than the CLAL cell. This suggests that pairing an unpatterned electrode with a patterned electrode significantly improves the unpatterned electrode's wetting within a coin-cell. The thick, unpatterned electrodes are expected to wet slowly without the aid of vacuum filling processes. Video 1 shows a simple experiment where Gen2 electrolyte is dropped onto the surface of a pristine electrode and a laser patterned electrode. The electrolyte dropped onto the pristine electrode pools in place, demonstrating how slow the electrolyte wetting and wicking process is at ambient pressures. During coin-assembly, this pooled electrolyte may be pushed out from between the two pristine electrodes where it will settle around the edges of the cell. This is expected to significantly reduce the pristine electrode's rate and degree of wetting
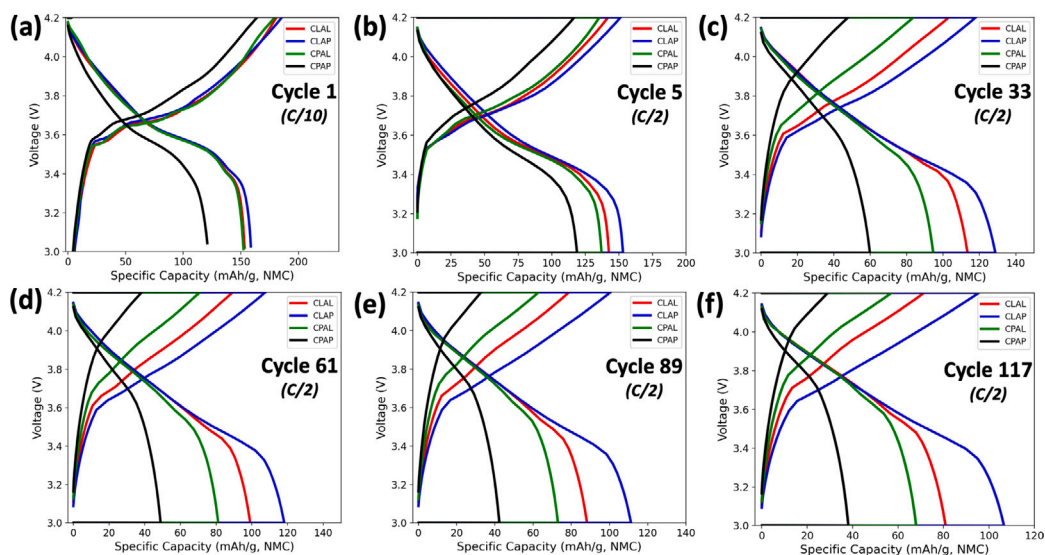
Fig. 5. Constant-current voltage profile of select cycles during a 100-6C cycle fast charge test.

within the CPAP coin cell. Conversely, the electrolyte dropped onto the surface of the laser patterned electrode quickly spreads laterally along the direction of its laser-patterned channels (Video 1). The laser-patterned electrodes are expected to wet through a two-step process. First, electrolyte quickly spreads across the electrode's micro-structured surface, filling its channels. Next, the electrolyte will slowly diffuse from the saturated channels into the bulk of the electrode. Concurrently, excess electrolyte held within the laser-patterned channels may also diffuse across the separator and into the opposing electrode. As electrolyte is slowly wicked out of the saturated channels and into the bulk of both electrodes, additional electrolyte from the perimeter of the flooded coin-cell is quickly drawn into the channels, replenishing them. By serving as rapidly refilling wells of excess electrolyte, the laser patterned channels may promote quick, uniform and complete wetting of both electrodes within a coin-cell. This could help explain the improved performance of the unpatterned electrodes in the CPAL and CLAP configurations.

The cycling performance of the coin-cells built with laser-patterned electrodes continues to diverge upon their second C/10 formation cycle. Of the patterned cells, the CLAP configuration obtained the largest CC charge capacity (165.8 mAh/g, NMC622). The CLAL and CPAL cells achieved CC charge capacities of 156.3 mAh/g (NMC622) and 153.4 mAh/g, respectively, significantly lower than the CLAP cell. This result appears to contradict a previous report on the laser patterning of similar graphite anodes and NMC622 cathodes, which showed considerably better cycling performance from anode patterning rather than cathode patterning [30]. Assuming comparable degrees of wetting, this variation in the low rate (C/10) performance is best explained by the n/p ratios of the laser patterned full cells.

The n/p ratio of each coin-cell configuration is listed in Table S9 along with an explanation of their estimation. The pristine electrodes of the baseline cell (CPAP) have an n/p ratio of 1.11. Patterning just the cathode (CLAP) increases the cell's n/p ratio to 1.24. In comparison to the CPAP baseline cell, the more cathode-limited CLAP cell would experience a reduced average degree of lithiation of its graphite anode materials and a larger average degree of delithiation of its NMC cathode materials during charging. This effect can be best observed in the cell's dQ/dV plot (Figure S9), where its third charge peak ($\approx$3.8 V), representing the formation of more highly lithiated graphite phases (Li_xC_6), is noticeably smaller than the other cells'. This trend of decreasing third peak height with increasing n/p ratio holds for all four cells tested. Despite its relatively large degree of NMC delithiation upon charging, the CLAP cell greatly outperformed the CPAP baseline cell,

achieving the largest first and second cycle specific charge capacities (187.4 mAh/g NMC, 167.3 mAh/g NMC) and coulombic efficiencies (86.0%, 99.2%) of any cell tested. This shows that any stresses on the cathode due to increased n/p ratio were relatively inconsequential in comparison to the improved wetting and Li-ion transport provided by the laser patterning.

When just the anode is patterned (CPAL), the cell's n/p ratio drops significantly below unity (0.92). In this case, the cell will be expected to exhaust its anode's capacity upon charging, leading to Li-plating regardless of the cycling rate. In fact, high voltage ($\approx$4.1 V) inflections in the CPAL cell's charge and discharge profiles (Fig. 5a) along with low coulombic efficiencies (85.2% - 1st cycle, 97.9% - 2nd cycle) indicate that the sub-unity n/p ratio gave rise to semi-reversible Li-plating during the initial C/10 formation cycles [26]. This shows that although laser patterning can drastically improve ion-transport in the anode, alleviating the concentration gradients that can lead to Li-plating, it is important to always consider the full cell's capacity balance (n/p) to prevent severely anode-limited electrode pairings.

Finally, the fully patterned CLAL cell was experimentally found to have an n/p ratio very near unity (n/p = 1.03). This can be explained by the slightly larger than expected mass losses during anode patterning compared to cathode patterning. Because the CLAL cell has an n/p ratio of $\approx$1, its anode will have to utilize the complete capacity of its graphite active materials upon full charge. This near unity n/p ratio could help explain why the CLAL cell under-performed in comparison to the CLAP cell. As the CLAL cell is fully charged, concentration gradients within the almost fully saturated anode could trigger cell voltage cutoff prior to complete charge acceptance from the cathode. This would explain the fact that the CLAL cell achieved a first cycle-charge capacity >3% smaller than the CLAP cell. Furthermore, pushing the graphite active materials to their lithiation limit could lead to irreversible capacity loss due to Li-plating, active material damage and interfacial reactions with the electrolyte. This hypothesis can be supported by the CLAL cell's decreased coulombic efficiencies (85.5% - 1st cycle, 98.3% - 2nd cycle) in comparison to the CLAP cell (86.0% - 1st cycle, 99.2% - 2nd cycle) during formation.

The electrochemical performance of all four cells continues to diverge over their first three C/2 cycles (Fig. 4). The CLAP cell maintains a large discharge capacity of 165.5 mAh/g (NMC), while the CLAL, CPAL and CPAP capacities drop to 153.1 mAh/g, 146.3 mAh/g and 133.3 mAh/g, respectively (Fig. 4b). Even at the relatively slow charge rate of C/2, the CPAP, CPAL and CLAL cells all show significant signs of capacity fading. The rate of capacity fade in the cells' first

three C/2 cycles trends well with their average coulombic efficiencies; 96.0% CPAP, 98.0% CLAL, 98.7% CLAL and 99.7% CLAP (Fig. 4d). The most rapid capacity degradation occurs in the baseline CPAP cell. This suggests that even at a C/2 rate, poor wetting and ion-transport limitations resulted in significant concentration polarization and Li-plating. The CPAP cell's 5th cycle voltage profiles (Fig. 5b) display large overpotentials supporting this hypothesis. The CPAL cell's relatively low capacity and rapid capacity fade can be explained by continued Li-plating as a result of its <1 n/p ratio. Once lithium has been irreversibly plated on an anode, it significantly increases the likelihood of continued plating during subsequent charges [54]. This is because the dead Li-deposits on the anode's surface greatly reduce the activation barrier for Li-plating compared to the pristine surface. Furthermore, Li-plating reduces the anode's porosity, slowing Li-transport near the electrode's surface, which can drive additional plating. Therefore, even if irreversible capacity loss pushed the CPAL cell's functional n/p ratio above unity, it could still continue to plate lithium despite the wetting and ion-transport benefits of its laser patterned anode. The reduced capacity and poor coulombic efficiency of the CLAL cell can also be attributed to its n/p ratio. Because very little capacity fading was observed in the CLAP cell where more severe polarization would be expected due to its lack of anode patterning, it can be concluded that the CLAL cell's reduced performance is not related to electrode wetting or ion-transport but is instead a direct consequence of its near unity n/p ratio. The outstanding performance of the CLAP cell can therefore be linked to its large n/p ratio as well as its improved wetting and ion-transport over the pristine (CPAP) case.

During their first 10-min 6C CC–CV fast-charge cycle, the CLAP, CLAL and CPAL cells significantly outperform the baseline CPAP cell achieving areal discharge capacities of 1.91 mAh/cm^2 (84 mAh/g, NMC), 1.67 mAh/cm^2 (74 mAh/g, NMC), 1.73 mAh/cm^2 (68 mAh/g, NMC) and 1.11 mAh/cm^2 (43.9 mAh/g, NMC), respectively. This represents a nearly 100% increase over the CPAP baseline in achievable discharge capacity following a 10-min fast-charge, a metric very relevant to real-world applications such as EVs. The data shows that patterning either the anode (CPAL), the cathode (CLAP), or both electrodes (CLAL) results in significant improvements to the coin-cell's fast-charge performance. This result was unexpected and suggests that in addition to improvements in ion-transport though the electrodes, the excess electrolyte held within the laser patterned channels plays a critical part in the fast-charge performance of these coin-cells.

The time each coin-cell took to reach its upper voltage cutoff (4.2 V) during 6C CC charging and the corresponding areal capacities are plotted in Figure S8a. The cells' 1st and 3rd 6C CC charge-step voltage profiles are plotted in Figures S8b & S8c. During the 1st fast-charge cycle, the baseline cell reached its upper voltage-limit in only 8 s due to extreme polarization, while the three patterned cells (CLAL, CLAP, CPAL) achieved CC time-to-cutoff of around 19 s. This represents an initial improvement in CC charge acceptance of 137% over the CPAP baseline case for each coin-cell containing patterned electrodes. However, these 6C charge steps correspond to only 0.14 mAh/cm^2 of CC capacity from the patterned cells and only 0.056 mAh/cm^2 for the CPAP cell, meaning 92%–96% of each coin-cell's total capacity was gained during the CV portion of its 10-min CC–CV fast-charge protocol. Laser patterning the thick electrodes, especially the anode, resulted in significantly reduced cell polarization during fast-charging (Figure S8a). This points to clear improvements in the cell's Li-ion diffusion, concentration gradients, and wetting with electrode patterning. After 10 cycles, the CLAP, CLAL, CPAL and CPAP cell's time-to-cutoff values stabilized to 26.0, 22.8, 17.0 and 8.4 s, respectively. This corresponds to 300% and 270% improvements over the CPAP baseline for the CLAP and CLAL cells, respectively.

Similar to their time-to-cutoff values, each cell's capacity begins to stabilize over their first 10 fast-charge cycles. The CPAP and CPAL cells experience significant capacity fading during these cycles. Sharp drops in the cell's coulombic efficiencies suggest that this rapid capacity

fading is the result of intense irreversible Li-plating during 6C fast-charging. Not only is this Li-plating leading to significant Li-loss in the cell, its clogging of the anode's surface is permanently restricting the cell's ion-transport capabilities, reducing its achievable fast-charge capacity over the set 10 min time frame. Conversely, the CLAL and CLAP cells show relatively stable capacities during these initial cycles. Interestingly, while the CLAL cell under-performed in comparison to the CLAP cell at slow (C/2) rates, both cells maintain relatively stable discharge capacities 1.75 mAh/cm^2 ($\approx$77 mAh/g, NMC) following 6C CC–CV fast-charging. This suggests that slow Li-ion transport into the CLAP cell's thick pristine anode limits its 6C CC–CV charge acceptance over a 10 min time frame.

After completing their first 25 (6C) CC–CV fast-charge cycles, the cells were again cycled at C/2 (CC–CV) to check their state-of-health. Fig. 4c shows that after just 25 6C fast-charge cycles, the CPAP cell's accessible capacity dropped by more than 50%. The CLAP, CLAL and CPAL cells retained 79.3%, 75.5% and 71.7% of their initial capacities, respectively. This shows that laser patterning either electrode has a significant impact on a coin cell's capacity retention following fast-charging. The majority of each cell's capacity loss is expected to be the result of irreversible Li-plating and electrolyte decomposition during fast-charging. Overpotentials in each cell's C/2 CC charging voltage (Fig. 5c) scale roughly with their capacity loss which would support this hypothesis. Of the patterned cells, the CPAL cell experienced the largest capacity loss (28.3%) after 25 6C fast-charge cycles. This indicates that despite improved wetting and ion-transport through its laser patterned anode, dead-Li deposited during initial charges (n/p < 1) gave rise to prolonged irreversible Li-plating during 6C fast-charging. This mechanism may also explain the CLAL cell's accelerated capacity fade in comparison to the CPAL cell, which showed no clear signs of early life Li-plating.

Over the following three 6C fast-charge steps, each cell showed relatively stable discharge capacities (Fig. 4). However, all four cells showed continued capacity loss and proportional charge voltage overpotential growth (Fig. 5) in each subsequent C/2 checkup step. This shows that while the cells continued to experience irreversible capacity loss with fast-charge cycling, the cells' achievable capacity over a 6C time frame remained relatively unaffected. This suggests that beyond the initial 10 fast-charge cycles, impacts to the electrodes' ion-transport capabilities are relatively gradual.

Upon completion of the 100 cycle fast-charge test, the CLAP, CLAL, CPAL and CPAP cells maintained reversible fast-charge capacities of 1.47 mAh/cm^2 (65.2 mAh/g, NMC), 1.28 mAh/cm^2 (56.5 mAh/g, NMC), 1.08 mAh/cm^2 (42.5 mAh/g, NMC) and 1.09 mAh/cm^2 (28.2 mAh/g, NMC), respectively, while retaining 65.5% (CLAP), 53.7% (CLAL), 47.4% (CPAL) and 30.0% (CPAP) of their initial C/2 capacities (Table 3). This result shows that laser patterning is a powerful tool to improve the achievable fast-charge capacity and capacity retention of thick, commercially relevant electrodes within coin cells by enhancing their ion-transport and wetting. It also shows that while laser patterning is an extremely effective technique, careful pattern designs ensuring appropriate n/p ratios is especially important for the long term cell health. Future work will expand upon the observations of Zheng et al. and investigate in detail how various laser pattern geometries change with cycling [55], so that optimal patterns can be designed to account for clogging due to irreversible volumetric expansion, Li-plating or SEI buildup.

3.3.2. Capacity loss and Li-plating

To confirm that the cells' early-life capacity fade was the result of Li-plating prior to 6C fast-charging, an identical set of coin-cells were cycled through their first three C/10 formation cycles and three C/2 capacity benchmarking cycles, fully discharged to 3.0 V (I < C/20) and disassembled for postmortem analysis. Digital images of these cells' anodes are presented in Figs. 6a–d. The anodes were washed in a fresh salt-free electrolyte solvent-blend (EC:EMC, 3:7 w/w) prior to imaging.
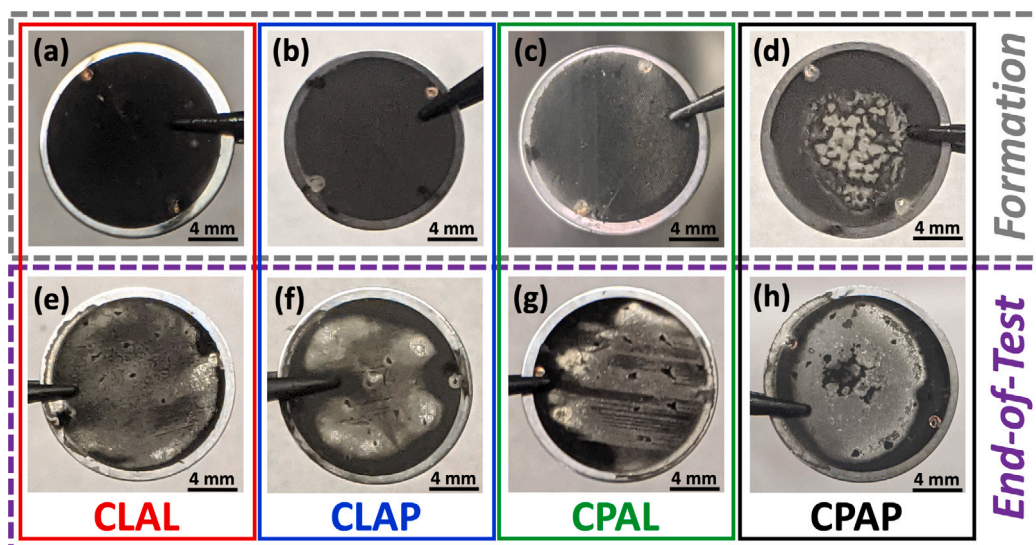
Fig. 6. Postmortem images of patterned and unpatterned anodes cycled in various coin cell configurations after completing (a–d) C/10-C/2 formation process and (e–h) 100-6C cycle fast charge test.

Fig. 6d verifies that the CPAP cell experienced significant lithium plating during its initial cycles. Dead lithium was also observed on the surface of the CPAL cell (Fig. 6c), although its intensity and morphology is noticeably different than the deposits on the CPAP anode. This morphological difference may be attributed to the underlying mechanism driving the Li-plating on each anode. For the CPAP cell, incomplete wetting and Li-ion transport limitations led to intense cell polarization and plating even at relatively slow C/2 rates. However, the Li-plating observed in the CPAL cell can be attributed to its sub-unity n/p ratio resulting in uniform Li nucleation across the anode's surface. No matter its morphology, the presence of dead Li on the surface of these anodes will certainly influence its subsequent fast charge cycling as it reduces ion-transport into the electrode and promotes the plating of additional Li. No obvious Li deposits could be seen on the surface of either the CLAL or CLAP cell's anodes after their first six cycles.

As discussed in the previous section, all four coin cells experienced significant capacity fade following their first 25 cycle 6C CC–CV fast-charge step. Much of this capacity loss occurred during the first ten fast-charge cycles, aligning with significant dips in the cells' coulombic efficiencies (Fig. 4d). Evidence that this rapid capacity loss is linked to intense Li-plating can be found in the cells' rest-step voltage relaxation curves following 6C fast-charging. After a typical charge, a cell's rest voltage is expected to relax quasi-exponentially as polarization in its electrodes and electrolyte homogenizes (Figure S10a). However, if fast-charging induces significant Li-plating, some of this lithium can be chemically intercalated back into the anode's graphite particles causing an inflection or plateau in its rest-voltage relaxation curve [56]. Figure S10b shows a non-exponential inflection in the CPAP cell's rest-voltage following its first 6C fast-charge. To accentuate the intercalation plateaus, the derivative of the rest-voltage (dOCV) is plotted vs time (Figure S11). A large inflection is visible in the CPAP cell's dOCV profile following its first 6C fast-charge. Small inflections are also observed in the CLAL, CLAP and CPAP cells' dOCV curves despite their rather featureless rest-voltage profiles (Figure S10b). This highlights the sensitivity of the dOCV technique and shows that all four cells experienced some degree of Li-plating on their initial 6C fast-charge. Inflections in cells' dOCV profiles remain visible until their 9th cycle, aligning with the stabilization of their discharge capacities and coulombic efficiencies. Previous reports have shown that the dOCV peak time and magnitude increases approximately linearly with increasing Li-plating intensity [57]. The CPAP cell's large dOCV peak centered around 450 s indicates that this cell experienced significantly more Li-plating than the cells containing laser patterned electrodes. This agrees
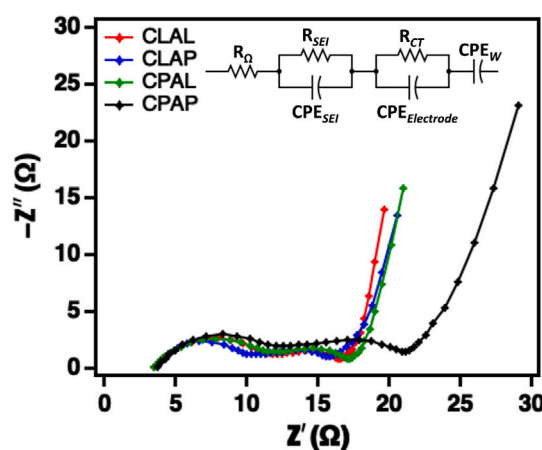

Fig. 7. (a) Electrochemical impedance spectroscopy (EIS) Nyquist plot (1 MHz–10 mHz) of fully discharged coin cells after completing a 100-6C cycle fast charge test.

Table 4
Resistances calculated from equivalent circuit fitting of EIS spectra.

Cell	R_{Ω} (Ω)	R_{SEI} (Ω)	R_{CT} (Ω)
CPAP	3.74	9.81	11.4
CPAL	3.51	8.9	6.75
CLAP	3.7	7.04	6.87
CLAL	3.52	8.61	5.96

with the CPAP cell's extreme capacity loss (≈50%) following its first 25 fast-charge cycles. In fact, each cell's dOCV peak magnitude and time trends well with their 6C fast-charge coulombic efficiency as well as their irreversible capacity losses. This suggests that Li-loss due to irreversible Li-plating is a leading mechanism for capacity loss in the coin-cells during their initial fast-charge cycles.

After 100 6C CC–CV fast-charge cycles, the coin-cells irreversibly lost 70.0% (CPAP), 53.8% (CPAL), 47.1% (CLAL) and 34.5% (CLAP) of their initial C/2 capacities. Electrochemical impedance spectroscopy (EIS) measurements were made on the cells immediately upon their completion of the fast-charge cycling experiment. Each cell's Nyquist plot (Fig. 7) shows two depressed semicircles followed by a steep tail in the low frequency range. The Nyquist plot's high frequency intercept

represents the cell's ohmic resistance. The first (high frequency) semi-circle is typically associated with the solid electrolyte interphase (SEI) layer formed on the cell's anode, while the second (mid frequency) semicircle is related to the charge-transfer resistance and double-layer capacitance at the electrodes. The cell's low frequency tail represents the electrodes' solid-state diffusion characteristics. Each cell's impedance spectra was fit with the equivalent circuit depicted in Fig. 7. The individual resistances calculated from the equivalent circuit fittings are listed in Table 4. The cells' ohmic resistances (R_Ω) range from 3.51 Ω–3.74 Ω. This variation could be explained by small fluctuations in the coin cells' temperatures during testing. Conversely, the similarity of each cell's R_Ω represents consistent bulk contributions from their electrolyte, separators, electrode coatings and current collectors. Each cell's R_{SEI}, which represents impedance due to surface species such as SEI, trends with their capacity fade in Fig. 4 and overpotentials in Fig. 5. This supports the hypothesis that each electrode's primary capacity degradation mechanism was Li-loss due to Li-plating and subsequent SEI formation with cycling, which is further corroborated by the end-of-test postmortem photos (Fig. 6 e–h) that show significant deposits of dead-Li on the surface of each cell's anode. Conversely, the R_{CT} values, which represent charge transfer processes between the electrodes and electrolyte, do not appear to trend with the cell's achieved capacities or capacity losses with cycling. Instead, the cells' R_{CT} values decrease with increasing electrode patterning. For example, the pristine (CPAP) cell has the largest R_{CT} of all of the cells (11.4 Ω). When just one of the electrodes is patterned (CLAP, CPAL), this value drops to 6.8 Ω. When both electrodes are patterned (CLAL), it drops further to 5.96 Ω. This shows that electrode patterning can significantly influence an electrode's charge-transfer resistance. This effect could be attributed to improved access to the electrode's active materials with laser patterning as well as improvements in ion-transport and reduced concentration gradients.

3.3.3. Laser ablation and electrode wetting

To quantify the extent of electrode wetting within the coin-cells, a simple electrochemical impedance spectroscopy experiment was conducted. Room temperature EIS sweeps were periodically performed on CPAP, CPAL and CLAL coin cells immediately following their assembly. Nyquist plots of the coin cells' impedance spectra immediately following assembly (empty markers) and after 48 h resting at room temperature (solid markers) are plotted in Fig. 7a. The EIS sweeps show a single depressed semicircle in the high frequency region with a 45° Warburg diffusion tail followed by a vertical spike in the mid to low frequency regions. The degree of electrolyte wetting within the coin-cells over time was then determined by calculating their electrochemically active specific surface areas. During EIS analysis, an electric double-layer is created on the electrode surface wetted by electrolyte. The magnitude of this double-layer capacitance scales directly with the wetted surface area of the electrodes. To determine the cell's double-layer capacitance, each Nyquist plot was first fit with a modified Randles circuit (Fig. 8a). This equivalent circuit models the depressed semicircular region of the cells' Nyquist plots as a Faradaic charge-transfer resistance (R_{ct}) in parallel with a double-layer constant phase element (CPE_{DL}). The cell's double-layer capacitance (C_{DL}) was then calculated with the equation:

$$C_{DL} = R_{ct}^{\left(\frac{1-n}{n}\right)} Q^{(1-n)} \tag{1}$$

Where n and Q are the empirical phase constant and pseudocapacitance values of the constant phase element (CPE_{DL}), respectively. Using the double-layer capacitance (C_{DL}), the cell's wetted surface area can be calculated from

$$A = C_{DL} d \varepsilon_r \varepsilon_o, \tag{2}$$

where d is the charge layer separation, ε_r is the dielectric constant (relative permittivity) and ε_o is the permittivity of vacuum. Fig. 8b plots

the magnitude each cell's wetted surface area, normalized to the total electrode coating mass on both the anode and cathode, over 48 h. The specific wetted surface areas calculated with this EIS method match relatively well with values of similar electrode composites in the literature determined using the Brunauer–Emmett–Teller (BET) nitrogen adsorption method [58]. This supports the merit of this technique as a quick and easy method to track the approximate degree of wetting within a full-cell coin-cell following assembly.

The wetting data (Fig. 7b) shows significant and immediate improvements in electrode wetting with laser patterning, corroborating similar findings in the literature [21]. For example, while the fully patterned CLAL coin-cell achieved a specific wetted surface area of 2.95 m²/g just one hour after its assembly, it took the CPAP baseline cell two full days of resting to approach the same state. This gives credence to the hypothesis that the CPAP cell's pristine electrodes were critically under wetted by electrolyte during testing despite coin cell flooding and pre-cycling resting periods. The data also supports the hypothesis that pairing a pristine electrode with a patterned electrode significantly improves the pristine electrode's rate and degree of wetting within a coin-cell. Fig. 7b shows that the CPAL cell starts with a specific wetted surface area only slightly smaller than the CLAL cell, and that its wetted surface area grows rapidly nearly matching the CLAL cell's after only 24 h. This could be interpreted as the CPAL cell's patterned anode quickly wetting with electrolyte and pulling excess electrolyte from the edges of the cell into its laser patterned channels where it can then slowly diffuse across the separator and into the opposing pristine cathode. This experiment helps explain the poor performance of the CPAP baseline coin-cell and the better than expected performance of the CLAP and CPAL configurations. It also shows the incredible value of the laser patterning technique in reducing costly wetting times and formation processes during the manufacturing of cells with thick electrodes. In the future, soaking the electrode disks in vials of electrolyte prior to coin-cell assembly could help ensure more complete electrolyte wetting and thus better assessment of their high-rate performances. However, testing thick electrodes in pouch cells where vacuum filling steps can be administered may be a better approach.

3.3.4. Model fit

A pseudo-2D model was prepared in COMSOL Multiphysics (Section S2) and fit to the electrochemical performance of a CPAP coin-cell. Despite a good understanding of the thick electrodes' properties (porosity, tortuosity etc.), the model consistently overestimated the baseline coin-cell's fast-charge performance and could not be made to fit the experimental fast-charge data within reason. The divergence between the model and the experimental data grew larger when electrode patterning was considered. While experimental data showed electrode patterning resulted in extreme performance improvements over the baseline (100% improvement in 6C CC–CV fast-charge capacity, 300% improvement in cut-off time), the model predicted much more modest improvements (6% improvement in 6C CC–CV fast charge capacity and 10% improvement in cut-off time). The large discrepancy between the model predictions and experimental data can be explained by the fact that the model assumes perfect wetting of the thick (>100 μm) electrodes by the electrolyte. However, as shown in the previous section, the thick pristine electrodes could not be properly wetted within the CPAP coin-cell. Therefore, by only accounting for improvements in electrode tortuosity, the model fails to capture the impact of improved wetting within the patterned cells.

4. Conclusion

In exploring the possibility of unfavorable consequences of laser ablation on local electrode material properties, inspection with cross-section SEM, XRD, and EDS revealed little damage to the laser-impacted zones. SEM revealed that on the NMC cathode, some particles at
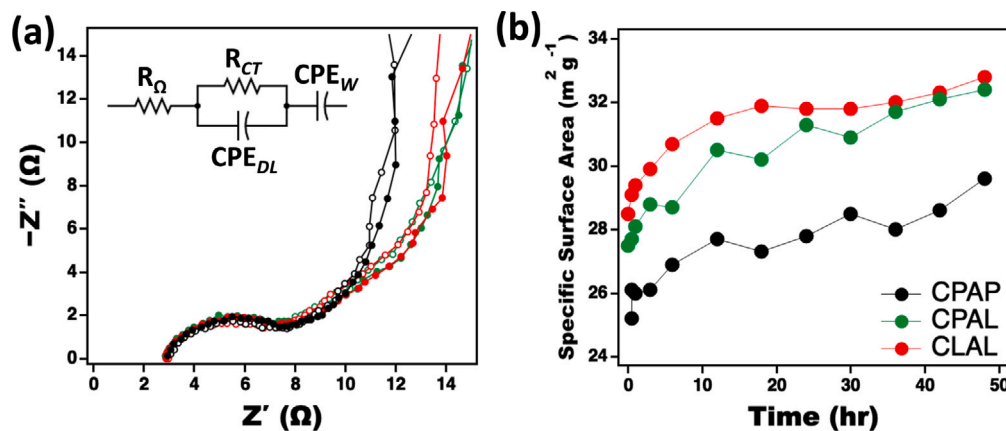
Fig. 8. (a) Nyquist plot of CPAP (black), CPAL (green) and CLAL (red) coin cell impedance spectra. Empty markers represent impedance response immediately after coin cell assembly, and solid markers represent final EIS scan 48 h after coin cell assembly. The Randles circuit the data was fit with is included for clarity. (b) Specific wetted surface area of CPAP, CPAL and CLAL coin cells over 48 h as calculated from room temperature coin cell impedance data. Each cell's wetted surface area is normalized to the total electrode coating mass on both the anode and cathode. (For interpretation of the references to color in this figure legend, the reader is referred to the web version of this article.)

the interface of the ablated pore and the electrode matrix were partially ablated, some of which were excessively cracked. However, the impact on performance of a small fraction of cracked or partially ablated particles is expected to be insignificant and no observable reduction in electrochemical performance of cells was observed. The variable operating parameters of laser systems such as pulse length, laser power, wavelength and repetition rates, provide opportunity to tune laser conditions to the different electrode chemistries and loadings that may have different thermal dissipation needs, thereby providing material-specific optimized ablation settings.

A clear and substantial improvement in the ability of cells with laser-ablated electrodes to charge quickly (in 10 min) was demonstrated. However, the respective contribution of each distinct electrode to improved cell performance was not equal. Rather, it was shown that while the best improvement in performance was achieved by ablating both electrodes, simply ablating one or the other electrode still leads to vast performance gains. An inherent drawback of laser ablation is material loss and since cell manufacturing costs are particularly sensitive to the expensive cathode materials, loss at the cathode is important to minimize. Demonstrating that substantial gains can be achieved without ablating the cathode has important economic consequences for scaleup and reducing loss during manufacturing.

Wetting of the electrodes was investigated by fitting a model to EIS data and extracting an estimate for the active (ionically connected) specific surface area. It was observed that laser-ablating just one electrode led to a significant increase in wetting of both electrodes. This result, in concert with multiphysics models that predicted more modest performance improvements for perfectly wet systems than what was achieved experimentally, supported a hypothesis that ablating one electrode provided additional local electrolyte to the other electrode, thereby improving wetting of both electrodes. Improvement of wetting was an additional benefit to performance beyond the anticipated reduced effective tortuosity of electrodes for fast charging. The laser-ablated cells also showed good life-cycle performance under fast charge conditions and upon disassembly following 120 cycles, showed reduced Li-plating on the graphite anode.

In summary, laser ablation can be applied to Li-ion electrodes with minimal impact to remaining chemistry, crystallographic, or morphological properties of the active material. Substantial performance benefits for fast charging can be achieved by ablating either electrode, while best performance is achieved after ablating both electrodes. Laser ablated electrodes improve rate capability, wetting, and reduce the risk of Li-plating during fast charging.

CRediT authorship contribution statement

Nathan Dunlap: Conceptualization, Investigation, Writing – original draft, Visualization. **Dana B. Sulas-Kern:** Investigation, Writing – review & editing. **Peter J. Weddle:** Methodology, Investigation, Writing – review & editing. **Francois Usseglio-Viretta:** Methodology, Investigation, Writing – review & editing. **Patrick Walker:** Investigation. **Paul Todd:** Investigation. **David Boone:** Supervision. **Andrew M. Colclasure:** Supervision. **Kandler Smith:** Supervision. **Bertrand J. Tremolet de Villers:** Conceptualization, Investigation, Writing – review & editing, Supervision, Project administration, Funding acquisition. **Donal P. Finegan:** Conceptualization, Investigation, Writing – original draft , Writing – review & editing, Supervision, Project administration, Funding acquisition.

Declaration of competing interest

The authors declare that they have no known competing financial interests or personal relationships that could have appeared to influence the work reported in this paper.

Acknowledgments

Appendix A. Supplementary data

Supplementary material related to this article can be found online at https://doi.org/10.1016/j.jpowsour.2022.231464.

References

[1] USABc goals for low-cost/fast-charge advanced batteries for EVs, 2020.

[2] D.L. Wood, J. Li, C. Daniel, Prospects for reducing the processing cost of lithium ion batteries, J. Power Sources 275 (2015) 234–242.

[3] D.P. Finegan, A. Quinn, D.S. Wragg, A.M. Colclasure, X. Lu, C. Tan, T.M.M. Heenan, R. Jervis, D.J.L. Brett, S. Das, T. Gao, D.A. Cogswell, M.Z. Bazant, M.D. Michiel, S. Checchia, P.R. Shearing, K. Smith, Spatial dynamics of lithiation and lithium plating during high-rate operation of graphite electrodes, Energy Environ. Sci. 13 (2020) 2570–2584.

[4] K.P.C. Yao, J.S. Okasinski, K. Kalaga, I.A. Shkrob, D.P. Abraham, Quantifying lithium concentration gradients in the graphite electrode of Li-ion cells using operando energy dispersive X-ray diffraction, Energy Environ. Sci. 12 (2019) 656–665.

[5] A.M. Colclasure, T.R. Tanim, A.N. Jansen, S.E. Trask, A.R. Dunlop, B.J. Polzin, I. Bloom, D. Robertson, L. Flores, M. Evans, E.J. Dufek, K. Smith, Electrode scale and electrolyte transport effects on extreme fast charging of lithium-ion cells, Electrochem. Acta 337 (2020) 135854.

[6] E.J. McShane, A.M. Colclasure, D.E. Brown, Z.M. Konz, K. Smith, B.D. McCloskey, Quantification of inactive lithium and solid–electrolyte interphase species on graphite electrodes after fast charging, ACS Energy Lett. 5 (2020) 2045–2051.

[7] A.M. Colclasure, A.R. Dunlop, S.E. Trask, B.J. Polzin, A.N. Jansen, K. Smith, Requirements for enabling extreme fast charging of high energy density li-ion cells while avoiding lithium plating, J. Electrochem. Soc, 166 (8) (2019) A1412–A1424.

[8] F.L. Usseglio-Viretta, W. Mai, A.M. Colclasure, M. Doeff, E. Yi, K. Smith, Enabling fast charging of lithium-ion batteries through secondary- /dual- pore network: Part I - Analytical diffusion model, Electrochem. Acta 342 (2020) 136034.

[9] W. Mai, F.L. Usseglio-Viretta, A.M. Colclasure, K. Smith, Enabling fast charging of lithium-ion batteries through secondary-/dual- pore network: Part II - numerical model, Electrochem. Acta 341 (2020) 136013.

[10] C.L. Cobb, M. Blanco, Modeling mass and density distribution effects on the performance of co-extruded electrodes for high energy density lithium-ion batteries, J. Power Sources 249 (2014) 357–366.

[11] C.L. Cobb, S.E. Solberg, Communication—analysis of thick co-extruded cathodes for higher-energy-and-power lithium-ion batteries, J. Electrochem. Soc. 164 (2017) A1339–A1341.

[12] J. Billaud, F. Bouville, T. Magrini, C. Villevieille, A.R. Studart, Magnetically aligned graphite electrodes for high-rate performance li-ion batteries, Nat. Energy 1 (2016) 16097.

[13] L. Li, R.M. Erg, J. Wang, J. Wang, Y. Chiang, Fabrication of low-tortuosity ultrahigh-area-capacity battery electrodes through magnetic alignment of emulsion-based slurries, Adv. Energy Mater. 9 (2019) 1802472.

[14] J.S. Sander, R.M. Erb, L. Li, A. Gurijala, Y.M. Chiang, High-performance battery electrodes via magnetic templating, Nat. Energy 1 (2016) 1–7.

[15] B.-S. Lee, Z. Wu, V. Petrova, X. Xing, H.-D. Lim, H. Liu, P. Liu, Analysis of rate-limiting factors in thick electrodes for electric vehicle applications, J. Electrochem. Soc. 165 (2018) A525–A533.

[16] S. Behr, R. Amin, Y.-M. Chiang, A.P. Tomsia, Highly-structured, additive-free lithium-ion cathodes by freeze-casting technology, Ceram. Forum Int. 92 (2015) E39–E43.

[17] B. Delattre, R. Amin, J. Sander, J.D. Coninck, A.P. Tomsia, Y.-M. Chiang, Impact of pore tortuosity on electrode kinetics in lithium battery electrodes: Study in directionally freeze-cast liNi$_{0.8}$co$_{0.15}$al$_{0.05}$o$_2$ (NCA), J. Electrochem. Soc. 165 (2018) A388–A395.

[18] R. Amin, B. Delattre, A.P. Tomsia, Y.-M. Chiang, Electrochemical characterization of high energy density graphite electrodes made by freeze-casting, Appl. Energy Mater. 1 (2018) 4976–4981.

[19] C. Huang, P.S. Grant, Coral-like directional porosity lithium ion battery cathodes by ice templating, J. Mater. Chem. 6 (2018) 14689–14699.

[20] Z. Liu, T.W. Verhallen, D.P. Singh, H. Wang, M. Wagemaker, S. Barnett, Relating the 3D electrode morphology to Li-ion battery performance; a case for LiFePO$_4$, J. Power Sources 324 (2016) 358–367.

[21] W. Pfleging, J. Pröll, A new approach for rapid electrolyte wetting in tape cast electrodes for lithium-ion batteries, J. Mater. Chem. A 2 (2014) 14918–14926.

[22] M. Mangang, H.J. Seifert, W. Pfleging, Influence of laser pulse duration on the electrochemical performance of laser structured LiFePO$_4$ composite electrodes, J. Power Sources 304 (2016) 24–32.

[23] J. Pröll, H. Kim, A. Poqué, H.J. Seifert, W. Pfleging, Laser-printing and femtosecond-laser structuring of LiMn$_2$o$_4$ composite cathodes for Li-ion microbatteries, J. Power Sources 255 (2014) 116–124.

[24] J.B. Habedank, J. Kriegler, M.F. Zaeh, Enhanced fast charging and reduced lithium-plating by laser-structured anodes for lithium-ion batteries, J. Electrochem. Soc. 166 (2019) A3940– A3949.

[25] K.-H. Chen, M.J. Namkoong, V. Goel, C. Yang, S. Kazemiabnavi, S.M. Mortuza, E. Kazyak, J. Mazumder, K. Thornton, J. Sakamoto, N.P. Dasgupta, Efficient fast-charging of lithium-ion batteries enabled by laser-patterned three-dimensional graphite anode architectures, J. Power Sources 471 (2020) 228475.

[26] J. Kriegler, L. Hille, S. Stock, L. Kraft, J. Hagemeister, J.B. Habedank, A. Jossen, M. Zaeh, Enhanced performance and lifetime of lithium-ion batteries by laser structuring of graphite anodes, Appl. Energy 303 (2021) 117693.

[27] J.B. Habedank, F.J. Günter, N. Billot, R. Gilles, T. Neuwirth, G. Reinhart, M.F. Zaeh, Rapid electrolyte wetting of lithium-ion batteries containing laser structured electrodes: in situ visualization by neutron radiography, Int. J. Adv. Manuf. Technol. 102 (2019) 2769–2778.

[28] T. Tsuda, N. Ando, S. Nakamura, Y. Ishihara, N. Hayashi, N. Soma, T. Gunji, T. Tanabe, T. Ohsaka, F. Matsumoto, Improvement of high-rate discharging performance of LiFePO$_4$ cathodes by forming micrometer-sized through-holed electrode structures with a pico-second pulsed laser, Electrochim. Acta 296 (2019) 27–38.

[29] T. Tsuda, N. Ando, K. Matsubara, T. Tanabe, K. Itagaki, N. Soma, S. Nakamura, N. Hayashi, T. Gunji, T. Ohsaka, F. Matsumoto, Improvement of high-rate charging/discharging performance of a lithium ion battery composed of laminated LiFePO$_4$ cathodes/ graphite anodes having porous electrode structures fabricated with a pico-second pulsed laser, Electrochem. Acta 291 (2018) 267–277.

[30] L. Hille, L. Xu, J. Keilhofer, S. Stock, J. Kriegler, M.F. Zaeh, Laser structuring of graphite anodes and NMC cathodes – proportionate influence on electrode characteristics and cell performance, Electrochem. Acta 392 (2021) 139002.

[31] J. Park, S. Hyeon, S. Jeong, H.-J. Kim, Performance enhancement of Li-ion battery by laser structuring of thick electrode with low porosity, J. Ind. Eng. Chem. 70 (2019) 178–185.

[32] J. Park, C. Jeon, W. Kim, S.-J. Bong, S. Jeong, H.-J. Kim, Challenges, laser processing and electrochemical characteristics on application of ultra-thick electrode for high-energy lithium ion battery, J. Power Sources 482 (2021) 228948.

[33] S. Johnson, D.B. Sulas, G.F. Kroeger, Laser cutting and micromachining for localized and targeted solar cell characterization, 2019 IEEE 46th Photovoltaic Specialists Conference (PVSC) (2019) 2753–2757.

[34] Battery test manual for electric vehicles, 2015.

[35] A. Heist, S.-H. Lee, Improved stability and rate capability of ionic liquid electrolyte with high concentration of LiFSI, J. Electrochem. Soc. 166 (2019) A1860.

[36] D. Lee, R. Patwa, H. Herfurth, J. Mazumder, High speed remote laser cutting of electrodes for lithium-ion batteries: Anode, J. Power Sources 240 (2013) 368–380.

[37] D. Lee, R. Patwa, H. Herfurth, J. Mazumder, Parameter optimization for high speed remote laser cutting of electrodes for lithium-ion batteries, J. Laser Appl. 28 (2016) 022006.

[38] C. Ronchi, R. Beukers, H. Heinz, J.P. Hiernaut, R. Selfslag, Graphite melting under laser pulse heating, Int. J. Thermophys. 13 (1992) 107–129.

[39] J. Steinbeck, G. Braunstein, M.S. Dresselhaus, T. Venkatesan, D.C. Jacobson, A model for pulsed laser melting of graphite, Int. J. Appl. Phys. 58 (1985) 4374.

[40] G. Braunstein, J. Steinbeck, M.S. Dresselhaus, G. Dresselhaus, B.S. Elman, T. Venkatesan, B. Wilkens, D.C. Jacobson, Pulsed laser melting of graphite, MRS Online Proc. Libr. 51 (1985) 233.

[41] D.H. Reitze, X. Wang, H. Ahn, M.C. Downer, Femtosecond laser melting of graphite, Phys. Rev. B 40 (1989) 11986–11989.

[42] T. Dallas, M. Holtz, Structural phase of femtosecond-laser-melted graphite, Phys. Rev. B 49 (1994) 796–801.

[43] A.I. Savvatimskiy, Measurements of the melting point of graphite and the properties of liquid carbon (A review for 1963–2003), Carbon 43 (2005) 1115–1142.

[44] X. Lu, N. Zhang, M. Jahn, W. Pfleging, H.J. Seifert, Improved capacity retention of SiO$_2$-coated LiNi$_{0.5}$mn$_{0.2}$co$_{0.2}$o$_2$ cathode material for lithium-ion batteries, Appl. Sci. 9 (2019) 3671.

[45] J. Li, H. Li, W. Stone, R. Weber, S. Hy, J.R. Dahn, Synthesis of single crystal LiNi$_{0.6}$mn$_{0.2}$co$_{0.2}$o$_2$ for lithium ion batteries, J. Electrochem. Soc. 164 (2017) A3529–A3537.

[46] H. Li, J. Li, X. Ma, J.R. Dahn, Synthesis of single crystal LiNi$_{0.6}$mn$_{0.2}$co$_{0.2}$o$_2$ with enhanced electrochemical performance for lithium ion batteries, J. Electrochem. Soc. 165 (2018) A1038.

[47] J. Li, J. Camardese, S. Glazier, J.R. Dahn, Structural and electrochemical study of the Li-Mn-Ni oxide system within the layered single phase region, Chem. Mater. 26 (2014) 7059–7066.

[48] X. Zhang, W.J. Jiang, A. Mauger, Qilu, F. Gendron, C.M. Julien, Minimization of the cation mixing in Li1+x(NMC)1-xO2 as cathode material, J. Power Sources 195 (2010) 1292–1301.

[49] F. Lin, I.M. Markus, D. Nordlund, T.-C. Weng, M.D. Asta, H.L. Xin, M.M. Doeff, Surface reconstruction and chemical evolution of stoichiometric layered cathode materials for lithium-ion batteries, Nature Commun. 3529 (2014) 1–9.

[50] P. Trucano, R. Chen, Structure of graphite by neutron diffraction, Nature 258 (1975) 136–137.

[51] B. Rethfeld, D.S. Ivanov, M.E. Garcia, S.I. Anisimov, Modelling ultrafast laser ablation, J. Phys. D: Appl. Phys. 50 (2017) 193001.

[52] F. Bourquard, T. Tite, A.-S. Loir, C. Donnet, F. Garrelie, Control of the graphite femtosecond ablation plume kinetics by temporal laser pulse shaping: effects on pulsed laser deposition of diamond-like carbon, J. Phys. Chem. C 118 (2014) 4377–4385.

[53] S. Johnson, D.B. Sulas, G.F. Kroeger, Theoretical approach to the laser-induced melting of graphite under different pressure conditions, Appl. Surf. Sci. 208 (2003) 61–70.

[54] P.P. Paul, V. Thampy, C. Cao, H.-G. Steinrück, T.R. Tanim, A.R. Dunlap, E.K. Dufek, S.E. Trask, A.N. Jansen, M.F. Toney, J.N. Weker, Quantification of heterogeneous, irreversible lithium plating in extreme fast charging of lithium-ion batteries, Energy Environ. Sci. 14 (2021) 4979.

[55] Y. Zheng, H.J. Seifert, H. Shi, Y. Zhang, C. Kubel, W. Pfleging, 3D silicon/graphite composite electrodes for high-energy lithium-ion batteries, Electrochim. Acta 317 (2019) 502–508.

[56] J.B. Habedank, J. Kriegler, M.F. Zaeh, Enhanced fast charging and reduced lithium-plating by laser-structrued anodes for lithium-ion batteries, J. Electrochem. Soc. 166 (2019) A3940.

[57] Z.M. Konz, E.J. McShane, B.D. McCloskey, Detecting the onset of lithium plating and monitoring fast charging performance with voltage relaxation, ACS Energy Lett. 5 (2020) 1750–1757.

[58] N.H. Kwon, The effect of carbon morphology on the $LiCoO_2$ cathode of lithium ion batteries, Solid State Sci. 21 (2013) 59–65.